Metall. Mater. Trans. A manuscript No.
(will be inserted by the editor)

Contraction twinning dominated tensile deformation and subsequent fracture in extruded Mg-1Mn (wt.%) at ambient temperature

A. Chakkedath · T. Maiti · J. Bohlen · S. Yi · D. Letzig · P. Eisenlohr · C.J. Boehlert

Received: November 16, 2017
DOI: 10.1007/s11661-018-4557-8

Abstract Due to their excellent strength-to-weight ratio, Mg alloys are attractive for applications where weight savings are critical. However, the limited cold formability of wrought Mg alloys severely restricts their widespread usage. In order to study the role that deformation twinning might play in limiting the elongation-to-failure (ε_f), in-situ tensile tests along the extrusion axis of Mg-1Mn (wt.%) were performed at 323 K, 423 K, and 523 K. The alloy exhibited a strong basal texture such that most of the grains experienced compression along their $\langle c \rangle$-axis during deformation. At 323 K, fracture occurred at about 10 % strain. Although basal, prismatic, and pyramidal $\langle c+a \rangle$ slip activity was observed along with extension twinning, contraction twinning significantly influenced the deformation, and such twins evolved into $\{1\,0\,\bar{1}\,1\}$–$\{1\,0\,\bar{1}\,2\}$ double twins. Crystal plasticity simulation showed localized shear deformation within the contraction twins and double twins due to the enhanced activity of basal slip in the reoriented twin volume. Due to this, the twin–matrix interface was identified to be a potential crack initiation site. Thus, contraction twins were considered to have led to the failure of the material at a relatively low strain, suggesting that this deformation mode is detrimental to the cold formability of Mg and its alloys. With increasing temperature, there was a significant decrease in the activity of contraction twinning as well as extension twinning, along with a decrease in the tensile strength and an increase in the ε_f value. A combination of basal, prismatic, and pyramidal $\langle c+a \rangle$ slip accounted for a large percentage of the observed deformation activity at 423 K and 523 K. The lack of contraction twinning was explained by the expected decrease in the critical resolved shear stress values for pyramidal $\langle c+a \rangle$ slip, and the improved ε_f values at elevated temperatures were attributed to the vanishing activity of contraction twinning.

Keywords double twinning · ductility

A. Chakkedath · T. Maiti · P. Eisenlohr · C.J. Boehlert (✉)
Chemical Engineering and Materials Science
Michigan State University
East Lansing, MI 48824, USA
Tel.: +1 517 353-3703
Fax: +1 517 432-1105
E-mail: boehlert@egr.msu.edu

J. Bohlen · S. Yi · D. Letzig
Magnesium Innovation Centre MagIC
Helmholtz-Zentrum Geesthacht – Zentrum für Material- und Küstenforschung GmbH
Max-Planck-Str. 1, D-21502 Geesthacht, Germany

1 Introduction

When it comes to light-weight material choices, magnesium (Mg) alloys provide an attractive solution due to their excellent specific strength compared to other commonly-used alloys [1,2]. However, the widespread acceptance of Mg and its alloys are restricted in high-volume manufacturing environments partially due to their limited cold formability. Due to this limitation, the processing of wrought Mg alloys is often performed at elevated temperatures for better formability, but this requirement results in an increased manufacturing cost. Thus, if Mg alloys are to be used more widely, it is critical to understand the mechanisms responsible for the ambient temperature deformation. One of the major factors that contribute to the limited cold formability of Mg alloys is their hexagonal crystallography, and the associated lack of sufficient independent slip systems that assist in uniform deformation [3]. In addition, several twinning deformation mechanisms also play a critical role in the limited ε_f at ambi-

ent temperatures. For example, fracture during compression along the ⟨c⟩-axis has been attributed to the excessive amount of shear caused by the activation of contraction/double twinning and the subsequent activation of slip within the twin volume [4–12].

Due to the lack of sufficient independent deformation mechanisms available for uniform deformation, wrought processing of Mg alloys often results in the formation of a crystallographic texture in which the ⟨c⟩-axis gets preferentially aligned perpendicular to the processing direction [13]. Further attempts to mechanically process material with this type of texture can place significant amount of compressive stress along the ⟨c⟩-axis. Neither of the two most easily-activated deformation systems in Mg (basal slip and extension twinning) can accommodate the strain originated during this type of loading condition. A slip system which can accommodate strain along the ⟨c⟩-axis (the pyramidal ⟨$c+a$⟩ slip system) is rarely activated at ambient temperatures due to its high critical resolved shear stress (CRSS) [14,15]. Thus, various contraction twinning-related mechanisms, which can accommodate strain along the ⟨c⟩-axis, are expected to activate when polycrystalline Mg alloys with a strong basal texture are deformed at ambient temperatures.

Various twinning modes, such as $\{10\bar{1}1\}$, $\{30\bar{3}4\}$, $\{10\bar{1}3\}$, $\{10\bar{1}5\}$, $\{10\bar{1}4\}$, $\{11\bar{2}4\}$, are activated when the ⟨c⟩-axis is placed under compression in Mg single crystals, and these twinning modes are often associated with crack initiation sites and fracture planes [4–10,16]. In addition, under similar loading conditions, double-twinned volumes, in which the primary twinning mode was reported to be either on $\{10\bar{1}1\}$ or $\{10\bar{1}3\}$ planes, and secondary twinning, which occur on $\{10\bar{1}2\}$ planes inside the primary twinned volume, have also been observed in Mg single crystals [10–12]. In such cases, void formation was reported along the twin–matrix interface, which has been identified as a fracture initiation site [11]. One possible explanation for this phenomenon is that this type of double twinning mechanism could result in the reorientation of the twinned volume assisting in the easy activation of basal slip, which in turn could result in the formation of localized shear bands, ultimately leading to shear failure [12].

Recent studies have reported the observation of a double twinning phenomenon in wrought polycrystalline pure Mg [17–19] and alloys such as Mg-3Al-1Zn (wt.%)[1] [16,17,20–23], Mg-6Al-1Zn [24], Mg-3Al-0.3Mn [25], Mg-3Al-0.4Mn [26,27], Mg-2Zn-0.5Mn [20], Mg-6Zn-0.5Zr [20], and Mg-0.2Ce [17]. Barnett [20] suggested that $\{10\bar{1}1\}$–$\{10\bar{1}2\}$ double twinning might cause shear failure at low strains due to the combined effect of strain softening and localized void formation. The formation of large surface steps, accompanied by narrow-banded $\{10\bar{1}1\}$–$\{10\bar{1}2\}$ twins, were reported in rolled Mg-3Al-1Zn after tensile deformation [22,28,29]. This suggests localized deformation within the double-twinned volume, which might assist in crack nucleation. Thus, the relatively low ε_f of Mg-3Al-1Zn at ambient temperature could be attributed to the formation of $\{10\bar{1}1\}$–$\{10\bar{1}2\}$ twins [20,22]. Niknejad et al. [24] observed the formation of transgranular cracks aligned with the $\{10\bar{1}1\}$–$\{10\bar{1}2\}$ double twin habit planes for Mg-6Al-1Zn, and they attributed this phenomenon to the shear localization within the double-twin volume, due to massive basal slip activity, leading to early transgranular crack/void initiation and subsequent fracture.

It was observed that the $\{10\bar{1}1\}$–$\{10\bar{1}2\}$ double twinning frequency decreased with an increase in temperature in extruded Mg-3Al-0.3Mn [25]. However, no detailed investigation of other slip activity was performed in that study. In Mg single crystals, it was observed that pyramidal ⟨$c+a$⟩ slip was prevalent at temperatures greater than 573 K, where the general twinning activity decreased with an increase in temperature, and this was attributed to the decrease in the CRSS values for non-basal slip at elevated temperatures [7,30]. Thus, non-basal slip systems, especially pyramidal ⟨$c+a$⟩ slip, are expected to be more active than contraction twinning at elevated temperatures [20].

It can be inferred from the previous studies that $\{10\bar{1}1\}$–$\{10\bar{1}2\}$ double twinning is partly responsible for the onset of failure of Mg alloys at ambient temperatures. It can be expected that at elevated temperatures, the CRSS of pyramidal ⟨$c+a$⟩ slip would become lower than that of contraction twinning and the decreased activity of contraction twinning might result in improved ε_f [20]. However, clear experimental evidence of this phenomenon is lacking, and its effect on the macroscopic behavior is not yet clear. In addition, a systematic study of the effect of temperature on the relative contribution of the different slip and twinning mechanisms is lacking in the literature. In this study, in-situ tensile experiments at different temperatures were performed to study the deformation behavior of extruded Mg-1 Mn (referred to as M1 according to ASTM standards for naming Mg alloys). The observation of double twinning in extruded M1, with a relatively fine grain size, at 323 K has been reported previously [31]. This is an extension of that study in which the effect of elevated temperature on the activation of double twinning is studied and discussed. In addition, crystal plasticity modeling and simulations, combined with the experimental results, were used to better understand the formation and evolution of $\{10\bar{1}1\}$–$\{10\bar{1}2\}$ double twinning in relation to other deformation modes and to fracture.

[1] henceforth all alloy compositions are provided in weight percent

2 Methods

2.1 Processing and alloy composition

The M1 alloy was gravity cast to produce a billet of 125 mm diameter. Subsequently, the billet was machined to a diameter of 93 mm and homogenized at 623 K for 15 h prior to extrusion. Indirect extrusion at a ratio of 1/30 was carried out at 573 K to produce round bars of 17 mm diameter. The chosen extrusion rate of 5.6 mm s^{-1} corresponds to a profile exit speed of 10 m min^{-1}. The chemical composition of the material, as measured by spark emission spectroscopy, was Mg-0.99 Mn (wt.%).

2.2 Sample preparation

Flat dogbone samples with a gage dimension of 3 mm wide by 2 mm thick by 10 mm long were electro-discharge machined from the extruded rod. One surface of the sample was mechanically polished to a mirror finish using 0.04 µm colloidal silica solution as a final step.[2] Mechanical polishing was followed by chemical polishing using a mixture of 100 mL methanol, 12 mL hydrochloric acid, and 8 mL nitric acid at room temperature for 2 s. The sample surface was etched for 1 s using a solution containing 60 mL ethanol, 20 mL water, 15 mL acetic acid, and 5 mL nitric acid.

2.3 In-situ testing

In-situ tensile tests were performed using a screw-driven tensile stage placed inside a TESCAN MIRA3 field-emission gun scanning electron microscope (SEM) with the tensile axis parallel to the material extrusion direction. Figure 2 shows the experimental setup with the tensile stage inside the SEM chamber.

A total of three tests were performed at 323 K, 423 K, and 523 K. The test temperature of 323 K was chosen in order to compare the results from this study with previous ones [32–36]. Specimen temperature was monitored using a fine-gage K-type thermocouple spot-welded to the side of the gage section. Radiant heating was provided by a tungsten-based heating element of 6 mm diameter placed just below the gage section and powered by a constant-voltage supply. A temperature constancy of ±3 K was maintained throughout the tests.

A constant crosshead displacement rate, corresponding to an engineering strain rate of 10^{-3} s^{-1}, was maintained during each test. Time, load, and crosshead displacement were recorded throughout the experiments. Local values of the (surface) tensile strain were derived from the relative displacements of obvious microstructural features on a secondary electron (SE) SEM image sequence acquired during each test. Stress relaxation occurred during these image acquisition periods, which lasted about 5 min.

Electron backscatter diffraction (EBSD) scans were performed on identical microstructural patches in the gage section both before and after deformation using an EDAX-TSL, Inc. system. The specimen surface was not further prepared for the EBSD scans after deformation as deterioration of the sample surface, due to the deformation, did not significantly affect the confidence in indexing the collected EBSD Kikuchi patterns. The EBSD data collection was performed using a step size of ≈ 1.5 µm for the microstructural patches in the gage section, and ≈ 0.15 µm for the individual twins. Post-processing clean-up procedures were performed on the raw data using EDAX OIM Analysis 6.1 software. Using the "Neighbor Confidence Index (CI) Correlation" clean-up procedure, the orientation of the erroneous data points, defined as points with a CI value below 0.03, were replaced with the orientation of the neighboring point that had the highest CI value. Using multiple iterations of the "Grain Dilation" clean-up procedure, any connected group of less than 5 pixels with a misorientation towards its neighborhood of greater than 5° was considered to be insufficient to be defined as a single grain, and the orientations of these points were reassigned to match the adjacent grain orientation. These clean-up procedures resulted in modifying less than 15 % of the total data points (in the undeformed specimens).

2.4 Slip/twin trace analysis

Active slip and twinning systems were identified based on the EBSD data and SE SEM images acquired during the tensile experiments. Linear surface steps observed in the SE images were attributed to that deformation system (slip or twinning, see Table 1 for all systems considered) for which the calculated trace of the slip or twin habit plane on the surface agreed most closely with the observed one. This surface plane trace is given by the cross-product between the (unit) normal vector of the surface and the deformation system plane rotated according to the particular grain orientation, as determined from EBSD.

[2] When exerting too much pressure during mechanical polishing, extension twins started to appear (see Fig. 1 for an example) predominantly within grains that have their ⟨*c*⟩-axis oriented perpendicular to the sample normal direction, i. e., those favorably oriented for extension twinning under the normal compression acting during polishing. Such twins did not evolve during the deformation experiments and were assumed to not influence the bulk mechanical behavior.

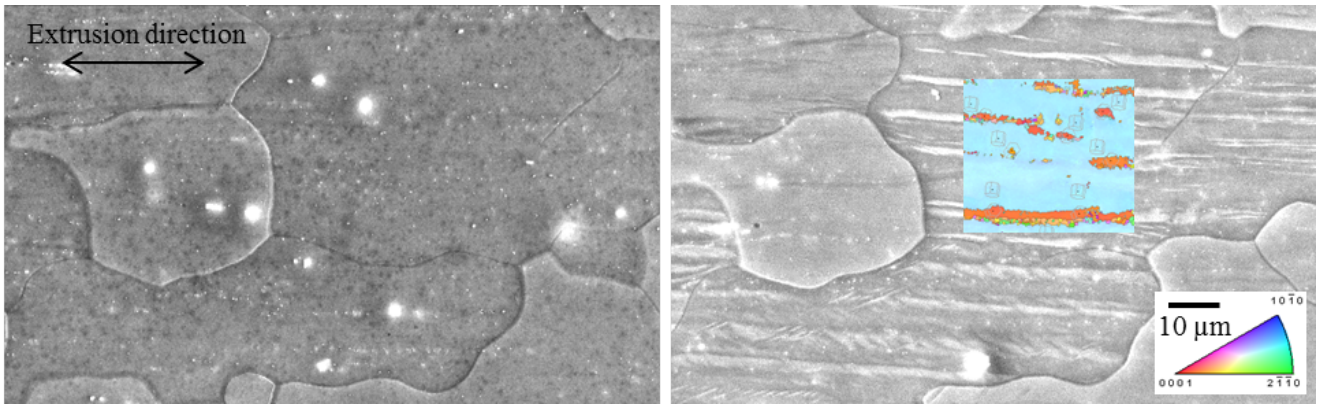

Fig. 1 – Secondary Electron (SE) photomicrographs of the as-extruded microstructure. Formation of thin extension twins in favorably oriented grains resulted from excessive polishing pressure. Right micrograph shows left area after (re)polishing under higher pressure. The insert in the right micrograph is an EBSD orientation map highlighting the twins.

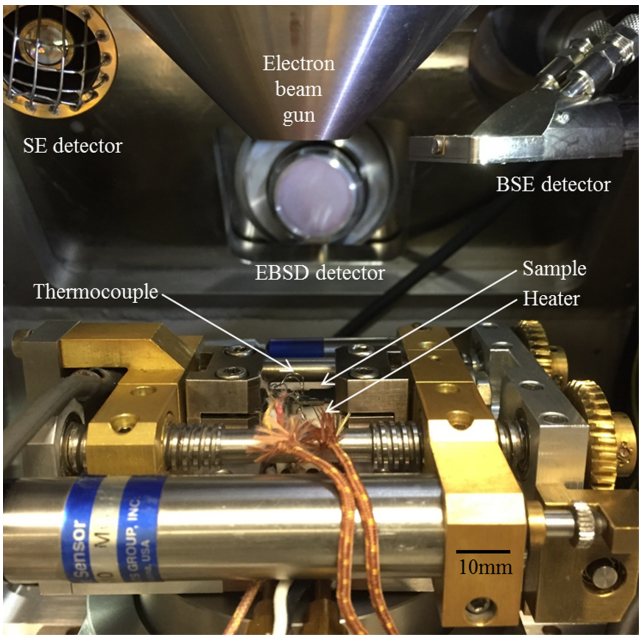

Fig. 2 – Temperature-controlled tensile stage placed inside a TESCAN MIRA3 scanning electron microscope chamber.

Table 1 – Slip/twin deformation modes considered for the trace analysis.

Deformation system	Variants	Plane	Direction
Basal slip	3	$\{0001\}$	$\langle\bar{2}110\rangle$
Prismatic slip	3	$\{01\bar{1}0\}$	$\langle\bar{2}110\rangle$
Pyramidal $\langle c+a\rangle$ slip	6	$\{11\bar{2}2\}$	$\langle\bar{1}\bar{1}23\rangle$
Extension twin	6	$\{10\bar{1}2\}$	$\langle\bar{1}011\rangle$
Contraction twin	6	$\{10\bar{1}1\}$	$\langle10\bar{1}2\rangle$

Twins identified using this approach were confirmed by checking the expected lattice reorientation against the measured orientation of the twinned region. Trace angle mismatches between experimental observations and the attributed deformation systems were within ±3°. Schmid factor values for all the deformation systems were calculated based on the respective grain orientation and assuming homogeneous uniaxial tension. Further details of this in-situ testing technique and the deformation characterization method can be found elsewhere [31–39]. The CRSS ratios of the different deformation modes versus the CRSS for basal slip were determined using the distribution of the slip/twin trace results and the methodology described in [40].

2.5 Crystal plasticity modeling and simulations

In order to better understand the deformation behavior, and in particular, the formation of the contraction twins and the $\{10\bar{1}1\}$–$\{10\bar{1}2\}$ double twins observed during the experiments, crystal plasticity simulations of isolated twins were performed. DAMASK [41,42] was used as (finite strain) material point model to describe the deformation response of these model microstructures. The deformation gradient $\boldsymbol{F} = \boldsymbol{F}_\mathrm{e}\boldsymbol{F}_\mathrm{p}$ at each material point was decomposed into an elastic $\boldsymbol{F}_\mathrm{e}$ and plastic $\boldsymbol{F}_\mathrm{p}$ component. The plastic velocity gradient follows as superposition of all slip activity

$$\boldsymbol{L}_\mathrm{p} = \dot{\boldsymbol{F}}_\mathrm{p}\boldsymbol{F}_\mathrm{p}^{-1} = \dot{\gamma}^{\xi}\boldsymbol{s}^{\xi}\otimes\boldsymbol{n}^{\xi} \tag{1}$$

where $\boldsymbol{s}$ and $\boldsymbol{n}$ are unit vectors along the slip direction and slip plane normal of deformation systems indexed by ξ. The stress resolved on each slip system follows from the elastic distortion as

$$\tau^{\xi} = 0.5\left[\mathbb{C}\left(\boldsymbol{F}_\mathrm{e}^{\mathrm{T}}\boldsymbol{F}_\mathrm{e} - \boldsymbol{I}\right)\right] : \left(\boldsymbol{s}^{\xi}\otimes\boldsymbol{n}^{\xi}\right) \tag{2}$$

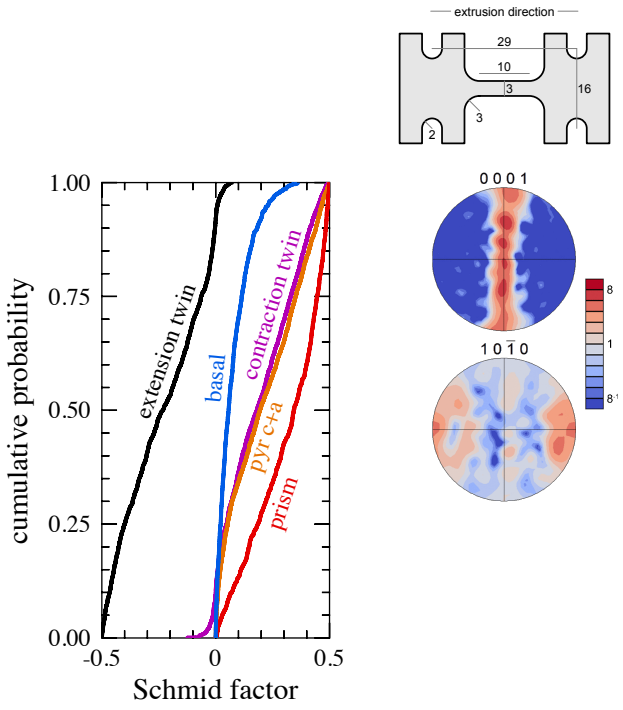

Fig. 3 – Geometry of tensile sample (top, dimensions in mm) and associated texture of extruded Mg-1 Mn (wt.%) in terms of ⟨0001⟩ and ⟨10$\bar{1}$0⟩ pole intensities (right, multiples of random) and distributions of Schmid factor values for different deformation systems based on unidirectional tension (left).

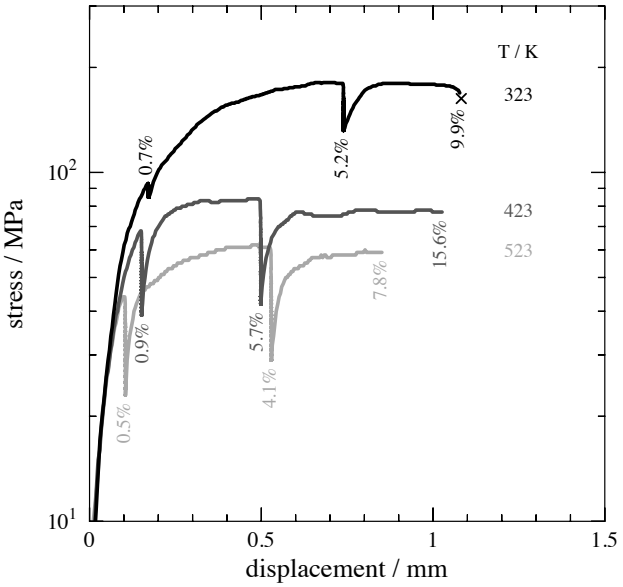

Fig. 4 – Stress versus displacement plots of the 3 samples tested depicting the temperature dependence of the mechanical response. Intermediate stress relaxations correlate with holding periods (zero displacement rate) during SE image acquisition. Corresponding strain levels, indicated on the plots, were determined from correlating distinct features between consecutive SE images (see sequences in Fig. 5) and deviate from the average sample strain. "×" indicates that the specimen failed (this occurred at 323 K only).

with $\mathbb{C}$ being the fourth-order stiffness tensor. The constitutive model used for the study is similar to the phenomenological description introduced by Peirce et al. [43] for cubic crystals. Shear on slip systems progresses at a rate

$$\dot{\gamma}^{\xi} = \dot{\gamma}_0 \left| \frac{\tau^{\xi}}{\tau^{\xi}_{\mathrm{cr}}} \right|^{n} \operatorname{sign} \tau^{\xi} \tag{3}$$

where $\dot{\gamma}_0 = 10^{-3}\,\mathrm{s}^{-1}$, $n = 20$. The state variables are the slip resistance τ^{ξ}_{cr} of each slip system, which evolve with shear γ as

$$\dot{\tau}^{\xi}_{\mathrm{cr}} = q^{\xi\zeta} h_0 \left(1 - \frac{\tau^{\zeta}_{\mathrm{cr}}}{\tau^{\zeta}_{\mathrm{sat}}} \right)^{a} \dot{\gamma}^{\zeta} \tag{4}$$

towards a saturation value $\tau^{\xi}_{\mathrm{sat}}$ according to a relationship given by Hutchinson [44]. Parameters used in the model are taken from [45].

3 Results

3.1 Texture and grain size

Figure 3 shows the texture of the extruded material, based on the EBSD measurement of an area containing approximately 1500 grains, in the form of ⟨0001⟩ and ⟨10$\bar{1}$0⟩ pole figures. The pole figures show a strong basal fiber texture, i.e. ⟨0001⟩ directions are mostly perpendicular to the extrusion direction (tensile direction). This type of texture, with intensities of about 10 times random, is common in conventional wrought Mg alloys, such as Mg-3Al-1Zn [13,35,46,47].

When loaded in tension parallel to the extrusion direction, such a texture favors prism slip over basal slip, with pyramidal ⟨$c+a$⟩ slip and contraction twinning falling in between these two and exhibiting about equal distributions of Schmid factors (see Fig. 3 left). As most grains are oriented with their ⟨c⟩-axis perpendicular to the tension direction, the shear stress resolved onto the (unidirectional) extension twinning systems turns out to be largely negative.

The average grain diameter was about 42 µm based on the E112-13 ASTM standard for grain size measurement [48]. Grain diameters ranged from 10 µm to 190 µm suggesting that grain growth may have occurred during the extrusion, which is not uncommon during wrought processing of M1 and other conventional Mg alloys [13].

Table 2 – Temperature dependence of tensile properties. Strains are estimated from the correlating surface features observed during the in-situ straining. (n/a: not applicable, as the sample was not taken to failure and and achieved approx. 8 % and 16 % strain at 423 Kand 523 K.) Temperature dependence of the tensile properties. Strains were estimated from the correlating surface features observed during the in-situ experiments. (NA: not applicable, as the sample was not taken to failure and and achieved approx. 8 % and 16 % strain at 423 K and 523 K.)

Deformation temp. / K	Yield stress YS / MPa	Ultimate stress UTS / MPa	Fracture strain / %
323	154	181	9.9
423	75	84	n/a
523	45	62	n/a

3.2 Mechanical characterization

The engineering stress versus displacement curves for the tensile tests performed at 323 K, 423 K, and 523 K are illustrated in Fig. 4. The sample tested at 323 K failed, while at the two other temperatures, the specimens remained intact. Stress relaxation at constant strain (labels give local values based on image correlation) occurred during image acquisition periods for which the displacement rate was reduced to zero. Table 2 lists the approximate yield strength (YS), ultimate tensile strength (UTS), and the maximum strain levels achieved for each experiment. The YS at 423 K and 523 K dropped to fractions of about 0.5 and 0.3, respectively, relative to that at 323 K, consistent with a similar reduction in YS with increasing temperature reported for conventional Mg alloys [35].

3.3 Slip and twin activity from surface trace analysis

During the holding periods marked by stress relaxation in Fig. 4, SE SEM images of three fixed areas, comprising a total of about 300 grains, were acquired. Figure 5 presents an exemplary sequence of one such area per deformation temperature. Linear traces, which appeared more frequently with increasing strain on the surface, could be identified as either basal, prismatic, or pyramidal $\langle c+a \rangle$ slip, or contraction twins, indicated by blue, red, orange, or purple lines, respectively. Extension twins usually did not result in noticeable surface features. Therefore, they were identified from corresponding sequences of the EBSD inverse pole figure (IPF) maps. Figure 6 gives examples of two extension twins appearing (as blueish regions) in the grains labeled "A" and "B". The observed crystallographic reorientation within such twinned regions, illustrated by hexagonal unit cells in Fig. 6, is very close to the theoretical 86° rotation about $\langle 1\,1\,\bar{2}\,0 \rangle$ with a twin plane $\{1\,0\,\bar{1}\,2\}$ [3], supporting the notion of extension twin activity.

About 90 % of all the observed surface traces could be matched with a unique deformation system, while the remainder had more than one possible match and was thus ignored. Figure 7 summarizes the combined distributions of (global) Schmid factors for basal, prismatic, and pyramidal $\langle c+a \rangle$ slip as well as for contraction and extension[3] twinning observed after the intermediate and final strain level (shown in Fig. 4) for all three temperatures. A number of observations were made.

1. All contraction twins were partly consumed by secondary extension twins, i. e. contain a fraction of double twinned volume.
2. Contraction and extension twinning together constituted about 3/4 of all observations at 323 K, but this fraction dropped substantially at 423 K, and reached zero for the highest deformation temperature of 523 K.
3. In terms of dislocation slip, the basal, prismatic, and pyramidal $\langle c+a \rangle$ families were observed in about equal proportion at the final strain levels (see Fig. 7 right).
4. In relation to the overall distributions of the Schmid factors (gray curves in Fig. 7, translated from the colored curves in Fig. 3), the observed activity clustered at the highest Schmid factor values. This clustering range was particularly narrow for prism slip (red curves) and, to a lesser degree, for contraction and extension twinning (purple and black curves). The exception to this general finding was pyramidal $\langle c+a \rangle$ slip, which showed a variation in observed Schmid factor value distributions (orange curves) with temperature. At 323 K, most of the observed Schmid factor values were relatively small, i. e. close to zero; at 423 K, the observations closely followed the underlying distribution of possible Schmid factor values; at 523 K, clustering occurred at relatively large Schmid factor values, similar to what was found for the other deformation modes.
5. The global Schmid factors for extension twinning were mostly negative since, given the texture, almost all grains were adversely oriented for this unidirectional deformation mode. Nevertheless, at 323 K, extension twins were observed at about half the frequency of that of contraction twins. At 423 K, both extension and contraction twin activity was largely diminished and both seemed to occur at about equal frequency.

3.4 Double twinning

During strain accumulation in the 323 K sample, $\{1\,0\,\bar{1}\,1\}$ contraction twins exhibited further (i. e., secondary)

[3] excluding double twinning, i. e., extension twinning within contraction twin volumes

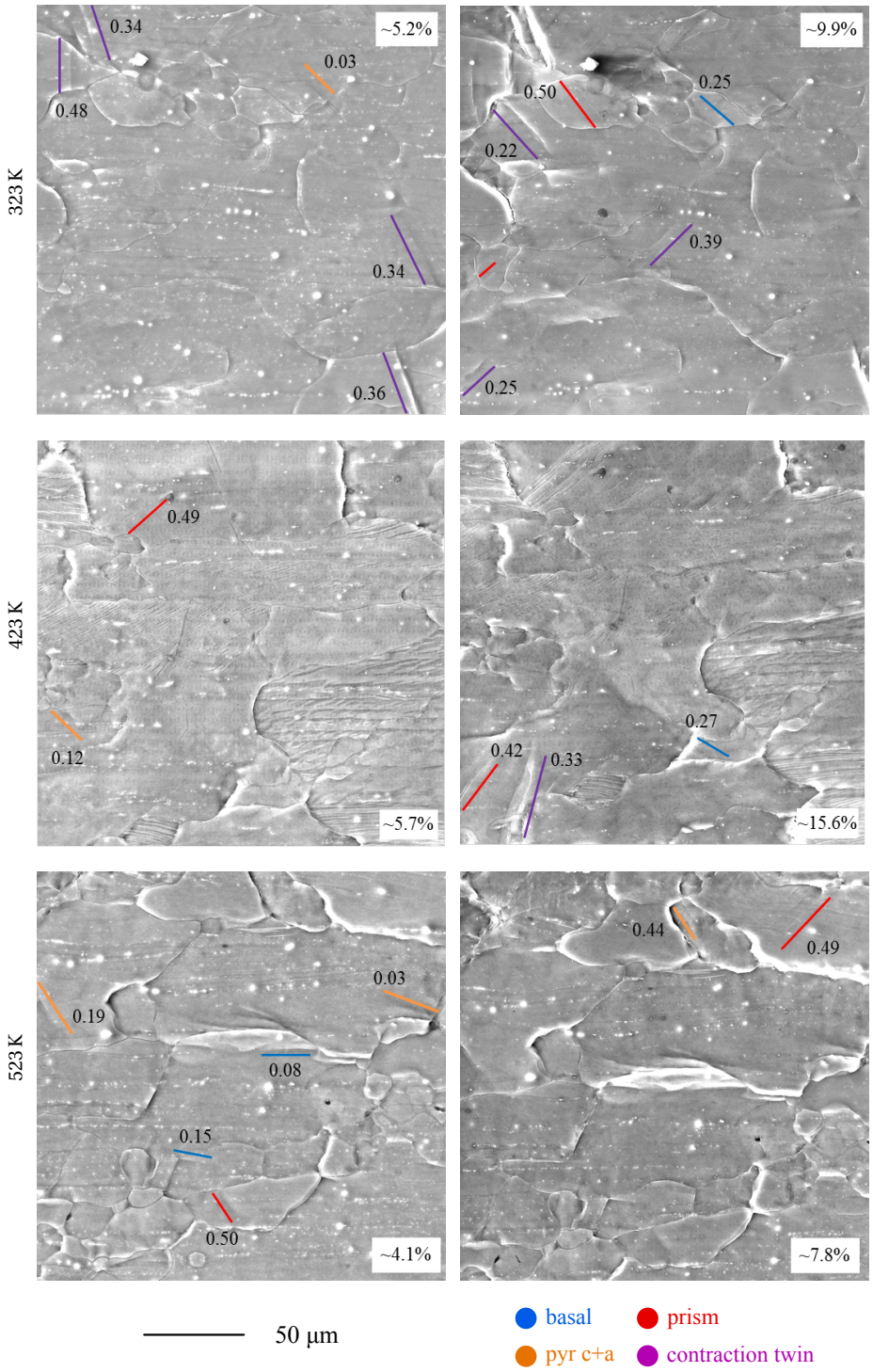

Fig. 5 – Pairs of secondary electron (SE) SEM images showing surface relief evolution with increasing (local) tensile strain for all three deformation temperatures. Colored lines with numbers indicate the identified deformation system trace and corresponding Schmid factor based on an assumed unidirectional tensile stress. Line coloring is listed at bottom right and follows same scheme as in Fig. 3 (left). Tensile axis and material extrusion direction are parallel to the scale bar shown at bottom left.

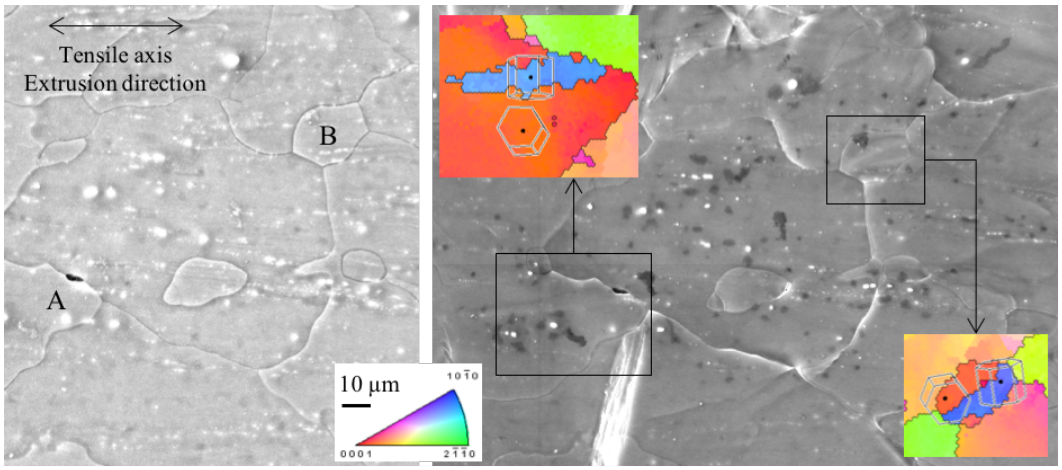

Fig. 6 – Observation of extension twin activity in grains marked "A" and "B" (left; undeformed) was difficult with the SE contrast but possible on the corresponding inverse pole figure map (IPF, right, blueish areas, after 9.9 % strain).

$\{10\bar{1}2\}$ extension twinning, resulting in $\{10\bar{1}1\}$–$\{10\bar{1}2\}$ double twins. In almost all cases the secondary $\{10\bar{1}2\}$ extension twin consumed a sizable fraction of the contraction twin volume.

Characterizing these events through EBSD was challenging, as the double-twinned regions were small in volume with high internal strain. Nevertheless, indexing was possible in some cases and regions of primary $\{10\bar{1}1\}$ contraction twinning and secondary $\{10\bar{1}2\}$ extension twinning could be identified. An example of such a case is pictured in Fig. 8 (bottom right), showing the SE SEM image and corresponding out-of-plane IPF map modulated by a grayscale map of Kikuchi band contrast (EBSD image quality). The blow-up from close to the upper end of the partly double-twinned volume illustrates in purple the boundary between the contraction twin (green area) and the parent orientation (magenta area), in black the boundary between original contraction twin and the secondary extension twin (again magenta), and in yellow the boundary between the double twin and the parent orientation (both are magenta areas). All colored boundary segments fell within 5° of their theoretical misorientation angle and axis; the +56° reorientation about $\langle 11\bar{2}0\rangle$ caused by the activation of the $\{10\bar{1}1\}$ contraction twin and the subsequent resorientation of an additional +86° about the same $\langle 11\bar{2}0\rangle$ axis (i.e., same plane of shear) caused by the subsequent activation of the $\{10\bar{1}2\}$ extension twin results in an effective rotation of −38° about $\langle 11\bar{2}0\rangle$ with respect to the matrix (Fig. 8 bottom right).

3.5 Fracture

For the sample deformed at 323 K, the fracture surface exhibited flat patches, which indicates a predominance of shear failure mode. The formation of contraction twins was associated with many visible surface steps (Fig. 8 top) evenly distributed over the entire gage section, but increasing in concentration closer to the final fracture location. Crack formation was observed along those surface steps with an increase in strain. One of the many secondary cracks in the vicinity of the final fracture location is magnified in Fig. 8 (bottom left). This one, and all similarly observed cracks, were found to be closely aligned with a trace consistent with contraction twinning (purple line in Fig. 8 bottom left).

4 Discussion

4.1 Characterization technique limitations

A limitation of the in-situ SEM testing is that only the surface behavior, which is likely to have somewhat different stress constraints than the bulk microstructure, is characterized. It should be noted that the more parallel the Burgers vector of a deformation system is to the sample surface, the more difficult slip lines of that system are to detect. Furthermore, if the slip was diffuse and not concentrated into well-defined slip bands, or if the magnitude of slip on a particular system was small and the slip bands were not well developed, the identification of the associated slip traces can be difficult. Therefore, activation of some of the deformation systems may not have been detected.

4.2 Activity of extension twinning

Even though the activation of extension twinning was not favored under the applied global stress state that mostly

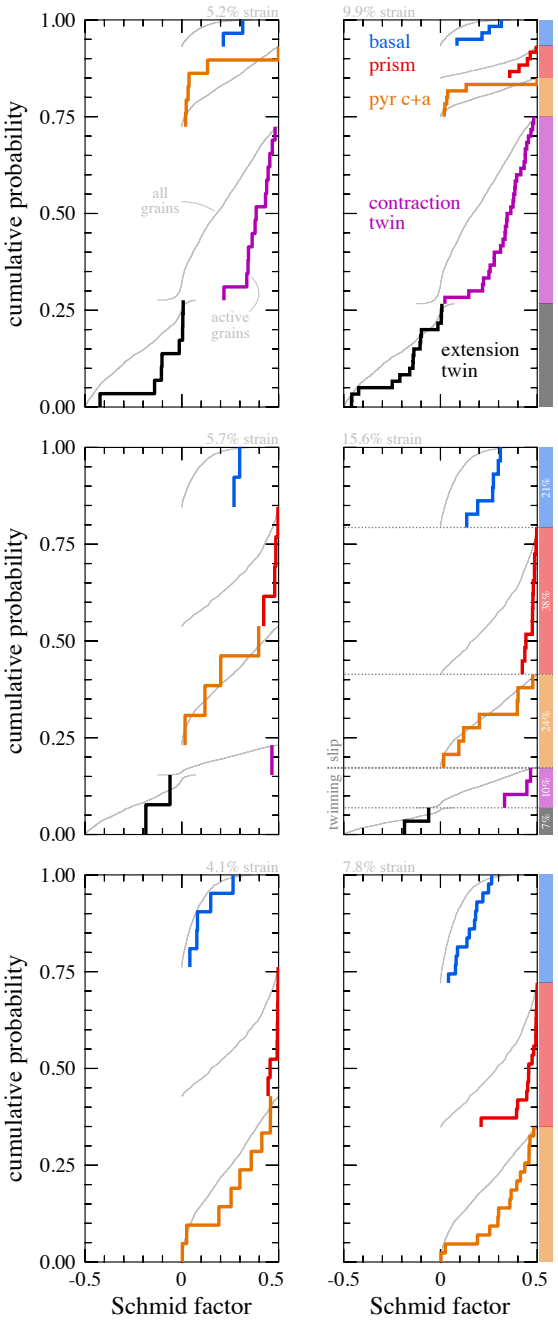

Fig. 7 – Cumulative probability distribution plots of the five evaluated deformation modes as a function of the Schmid factor for potential (thin, gray) and observed (thick, colored) deformation activity for the strain level indicated above each plot at 323 K, 423 K, and 523 K (top, middle, bottom). Schmid factor calculation assumes unidirectional (externally applied) stress.

resulted in compression (and not extension) along the ⟨*c*⟩-axis for the given material texture (see Fig. 3), a fraction of the observed deformation system activity was attributed to extension twinning. The majority of extension twinning was observed in grains that were close to being "properly" oriented for this unidirectional deformation mode, i. e., at only slightly negative Schmid factors (Fig. 7). Since a grain aggregate will likely experience different slip activity in different grains, the local mechanical boundary conditions are not necessarily equivalent to the globally applied (unidirectional) stress. Therefore, it is not difficult to rationalize that extension twinning can occur as a deformation accommodation mechanism in certain grains. For instance, the elongation along the tensile direction and associated lateral contraction of any of the relatively soft grains will be larger than that of other grains in their immediate neighborhood. A neighboring grain that happens to have its ⟨*c*⟩-axis pointing towards such a relatively soft grain (not unlikely for the given texture, see Fig. 3) would then have to accommodate the neighbor contraction by extending along its own ⟨*c*⟩-axis, demanding either pyramidal ⟨*c* + *a*⟩ slip or extension twinning. Occurrence of extension twinning has also been observed in polycrystalline pure Mg and Mg alloys under loading conditions (nominal compression along the ⟨*c*⟩-axis) that are comparable to the present work[17,18,21–23,49].

4.3 Temperature dependence of the critical resolved shear stress (CRSS)

In light of the virtual constancy of the relative contributions from the basal, prism, and pyramidal ⟨*c* + *a*⟩ slip families at all three temperatures, see Fig. 7, the relative reduction of the CRSS with increasing temperature appears to be very similar for all three families. With respect to their mutual ease of activation, the observation that prism slip is activated only at Schmid factor values close to the maximum of 0.5 could be interpreted as its CRSS being higher than that of either basal or pyramidal ⟨*c* + *a*⟩ slip, both of which exhibit activity for lower resolved shear stresses, i. e., over a more extended range of Schmid factors.

Contrary to slip, which was observed at all three deformation temperatures, the activity of contraction and extension twinning modes ceased between 423 K and 523 K. This suggests that the relative decrease with temperature of the CRSS values for contraction and extension twinning was less pronounced than that for the three slip families, such that twinning became relatively more difficult to activate at elevated temperatures.

Further support for the observed change from contraction twinning at 323 K to pyramidal ⟨*c* + *a*⟩ slip at 523 K as alternative deformation modes to accommodate strain

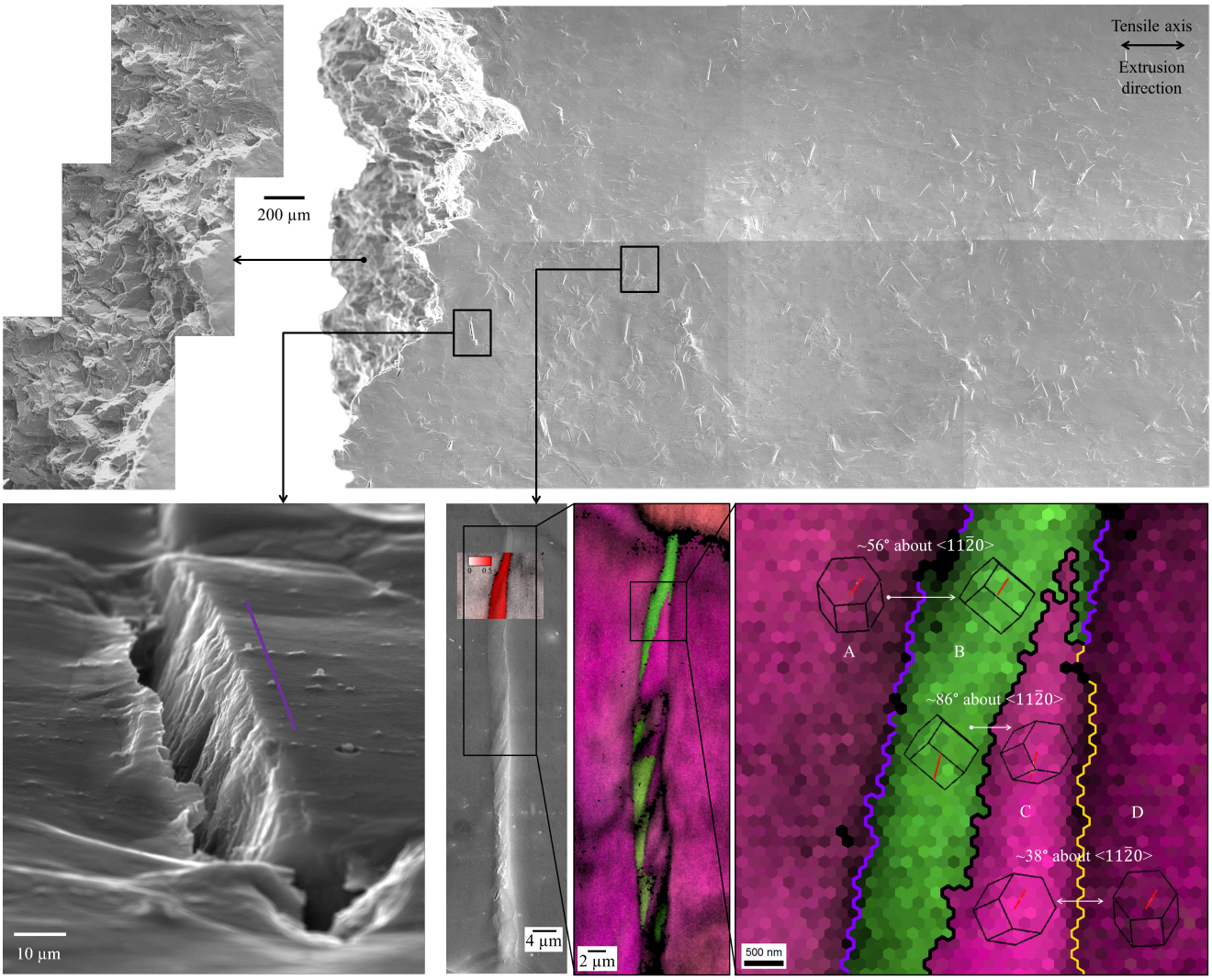

Fig. 8 – Overview of the fractured sample deformed at 323 K (top right) with an about 45° inclined view on the fracture surface (top left). Bottom left shows tilted view of a secondary crack near the main fracture location that aligns with the surface trace of a $\{1\,0\,\bar{1}\,1\}$ contraction twin (with global Schmid factor of 0.21) indicated by a purple line. Bottom center shows partly double-twinned volume about 1 mm away from the crack surface in SE contrast with a small area overlaid by a Schmid factor map for basal slip. Bottom right shows inverse pole figure maps with the surface normal direction modulated by grayscale EBSD image quality of an area containing the initial $\{1\,0\,\bar{1}\,1\}$ contraction twin (green, B) together with a secondary $\{1\,0\,\bar{1}\,2\}$ extension twin (magenta area, C, left of yellow boundary with untwinned parent grain, D, having same orientation as A).

along the $\langle c\rangle$-axis is provided in Fig. 9. In about 3/4 of all grains that only exhibited contraction twinning but no pyramidal $\langle c+a\rangle$ slip at 323 K (purple line in Fig. 9 left), the Schmid factor of the observed contraction twinning system is less than that of potential pyramidal $\langle c+a\rangle$ slip (diamonds falling to the right of purple line). This picture reverses at 523 K (Fig. 9 right), where the maximum Schmid factor of contraction twinning was larger than that of observed pyramidal $\langle c+a\rangle$ slip in about 1/2 of all grains that exhibit only pyramidal $\langle c+a\rangle$ slip. Hence, in both cases, there is no clear favorite among the two alternatives considering the maximum global Schmid factor, but the observed activity is clearly biased, suggesting that the CRSS for contraction twinning is relatively low at 323 K compared to pyramidal $\langle c+a\rangle$ slip, while the opposite holds at 523 K.

Statistical evaluation of all observed deformation activity derived from surface traces, following the methodology outlined in Reference [40], leads to the relative CRSS values depicted in Fig. 10 (top). According to this analysis, the only deformation mode at 323 K that has a lower CRSS value than contraction twinning is basal slip. Contrary to this result, studies on pure Mg single crystals under plane-strain compression at temperatures ranging up to 580 K (307 °C) [10] and 723 K (450 °C) [15] reported compression twinning to have a relatively high CRSS value at low tem-

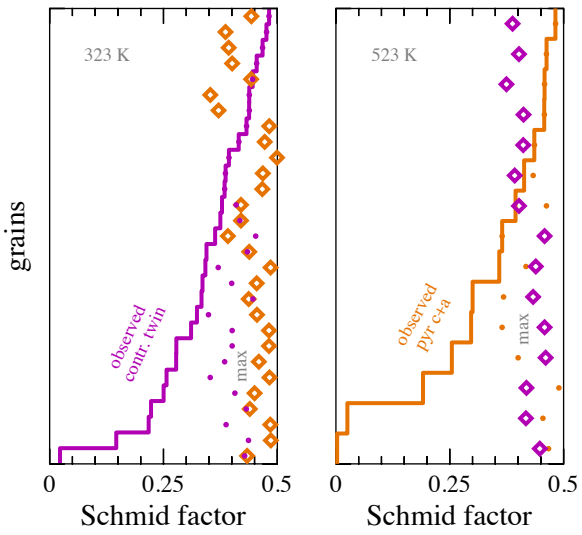

Fig. 9 – Comparison of Schmid factor values for contraction twinning (purple) and pyramidal $\langle c+a \rangle$ slip (orange) as alternative deformation modes that allow for $\langle c \rangle$-axis contraction. The solid line reflects the distribution of the Schmid factor values for the observed deformation system. The dots and diamonds show the maximum Schmid factors in each grain for the observed and alternative deformation mode, respectively.

peratures, and this CRSS value decreased with increasing temperature, consistent with other previous work[7]. That relative decrease with increasing temperature was similar to that found for pyramidal $\langle c+a \rangle$ slip, see Fig. 10 (bottom). The reason for this discrepancy remains unclear, but might be related to the effect of Mn additions on the stacking fault energy of Mg alloys, which has not been well documented to date.

4.4 Rationalization for double twin formation

Couling et al.[12] observed that $\{10\bar{1}1\}$–$\{10\bar{1}2\}$ double twins were formed by the activation of a $\{10\bar{1}2\}$ extension twin inside the $\{10\bar{1}1\}$ contraction twinned region. An explanation for this phenomenon was given by Koike et al.[49] and Ando and Sutou[22], who argue that the $\{10\bar{1}2\}$ extension twin within the $\{10\bar{1}1\}$ contraction twin was formed to accommodate and reduce the strain incompatibility between the primary $\{10\bar{1}1\}$ contraction twin and its surrounding matrix. The present study supports this notion of a necessary internal accommodation since not a single contraction twin volume without some secondarily-twinned fraction was observed.

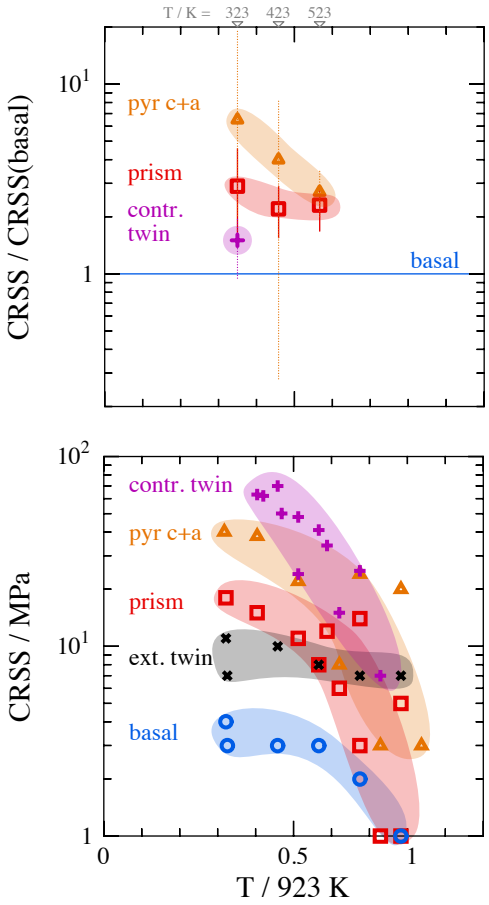

Fig. 10 – Temperature dependence of the CRSS for various deformation modes. Top figure presents CRSS ratios relative to basal slip (this work) and bottom figure collects CRSS values from references [5,7,9,10,15,30,50].

4.5 Interplay of contraction and double twinning with ε_f

The tension specimens tested at 423 K and 523 K exhibited higher elongation-to-failure ε_f values compared to that at 323 K (see Fig. 4). There is a clear correlation between this reduction of ε_f with decreasing temperature and the occurrence of mechanical twinning at low deformation temperatures (particularly 323 K). One explanation for this correspondence could be that dislocation slip, in particular on the basal plane, is strongly favored due to the reorientation of the lattice within each twinned volume. This local change in Schmid factor turns each twinned volume into a 'soft spot' that localizes shear and causes void initiation. This hypothesis can be supported by:

1. Clear surface ledges were only observed within the contraction twins that formed in the sample deformed at 323 K Fig. 8 (top and left).
2. The maximum global Schmid factor for basal slip was calculated for the matrix grains in the given texture and their most probable variant of extension, contrac-

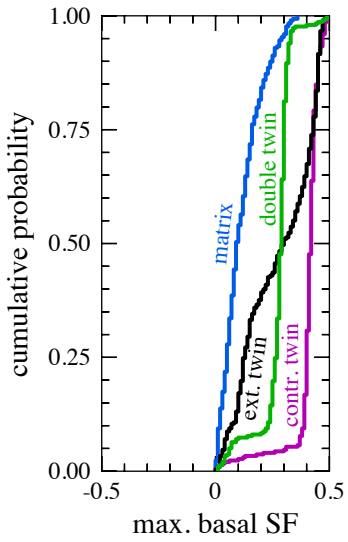

Fig. 11 – Cumulative probability distribution of the maximum Schmid factor for basal slip in the matrix grain population (blue) compared to its most probable extension (black) or compression (purple) twinned variant, i. e., the one with largest global Schmid factors for extension or compression twinning, as well as the $\{10\bar{1}1\}$–$\{10\bar{1}2\}$ double twin (green) population following from the postulated contraction twinned variant.

tion, and $\{10\bar{1}1\}$–$\{10\bar{1}2\}$ double twins (i. e. the variant that exhibited highest global Schmid factor for each twin type in the parent orientation). Figure 11 shows the cumulative probability distribution obtained from this calculation performed for the grain population included in Fig. 7. As shown in Fig. 11, the Schmid factor for basal slip in all three types of twinned regions (extension, contraction, and double twins) was relatively high compared to the matrix. This suggests that the mechanical twinning orients matrix grains in such a way that activation of basal slip becomes more favorable, and this combined with the low basal CRSS [14,15] creates dispersed regions of lower flow stress.

3. The tensile deformation behavior of a part of the contraction ("B") as well as double twinned region ("C") within the matrix grain ("A" or "D") shown in Fig. 8 (bottom right) was simulated using the crystal plasticity model described in Section 2.5 considering only the slip systems provided in Table 1. A fixed-width central region sandwiched between a matrix single crystal was oriented consistently with the habit plane of the observed contraction twin, as the primary contraction twin boundary did not change significantly with increases in strain during the experiments. Three simulations were performed with different lattice orientations selected for the central region: matrix, contraction twin, and $\{10\bar{1}1\}$–$\{10\bar{1}2\}$ double twin. The tensile axis was chosen in order to reflect the experimental setup, however, the four lateral faces were considered stress-free and not restricted by the bulk material as is the case in the real sample.

Figure 12 shows the stress and strain response for each simulation after 5.0 % strain. For the homogeneous matrix case, a homogeneous stress and strain field results. In both other cases, the unidirectional tensile stress in the twinned volume is lowered compared to the matrix while the strains are correspondingly larger. Specifically, the average strain (8 %) within the contraction twin is almost twice the prescribed overall strain (5 %), while the strain concentration was not as large in the double twin. This suggests that, after a contraction twin has nucleated, the entire twinned volume deforms similar to a shear band, where a contraction twin concentrates more strain than a double twin, consistent with the statistical evaluation of Schmid factors described above.

Comparing the accumulated shear from different slip systems (bottom three rows in Fig. 12), basal slip contributed almost all of the deformation in both twin types, consistent with the fact that basal slip has the lowest CRSS among all three slip families at ambient temperatures. Furthermore, the stronger concentration of basal slip observed in the contraction twin relative to the double twin is due to the fact that the most favorably oriented basal slip system features a higher Schmid factor in the former compared to the latter, for the particular matrix orientation chosen here.

Due to the relatively thin volume occupied by contraction twins or double twins, the dislocation mean free path is likely limited within them. The constitutive model used in the crystal plasticity simulations ignores this aspect, i. e. does not consider the slip incompatibility caused by the presence of a twin boundary. Ando and Sutou [22] reported the measured surface relief caused by $\{10\bar{1}1\}$ contraction twins and $\{10\bar{1}2\}$ extension twins to be smaller than that caused by $\{10\bar{1}1\}$–$\{10\bar{1}2\}$ double twins. The lower degree of plasticity in the former was attributed to a shorter slip length for basal slip inside those twin types compared to the double twinned volume [22,28]. Highly confined basal slip within an extension twin is shown in Fig. 13 for as-cast M1 alloyed with 0.5 Nd (8 % tensile strain, 323 K, average grain size of 0.36 mm, [51]).

Due to the relative softness of the central twinned volume, the localized strain causes a notable change in the simulated geometry (see back edge of top face in right two columns of Fig. 12). Despite the simplified boundary conditions in the simulations, the sense of the surface steps formed across the twinned regions in the simulations agrees with the experimentally-observed ones (see Fig. 8), i. e. the matrix on the right

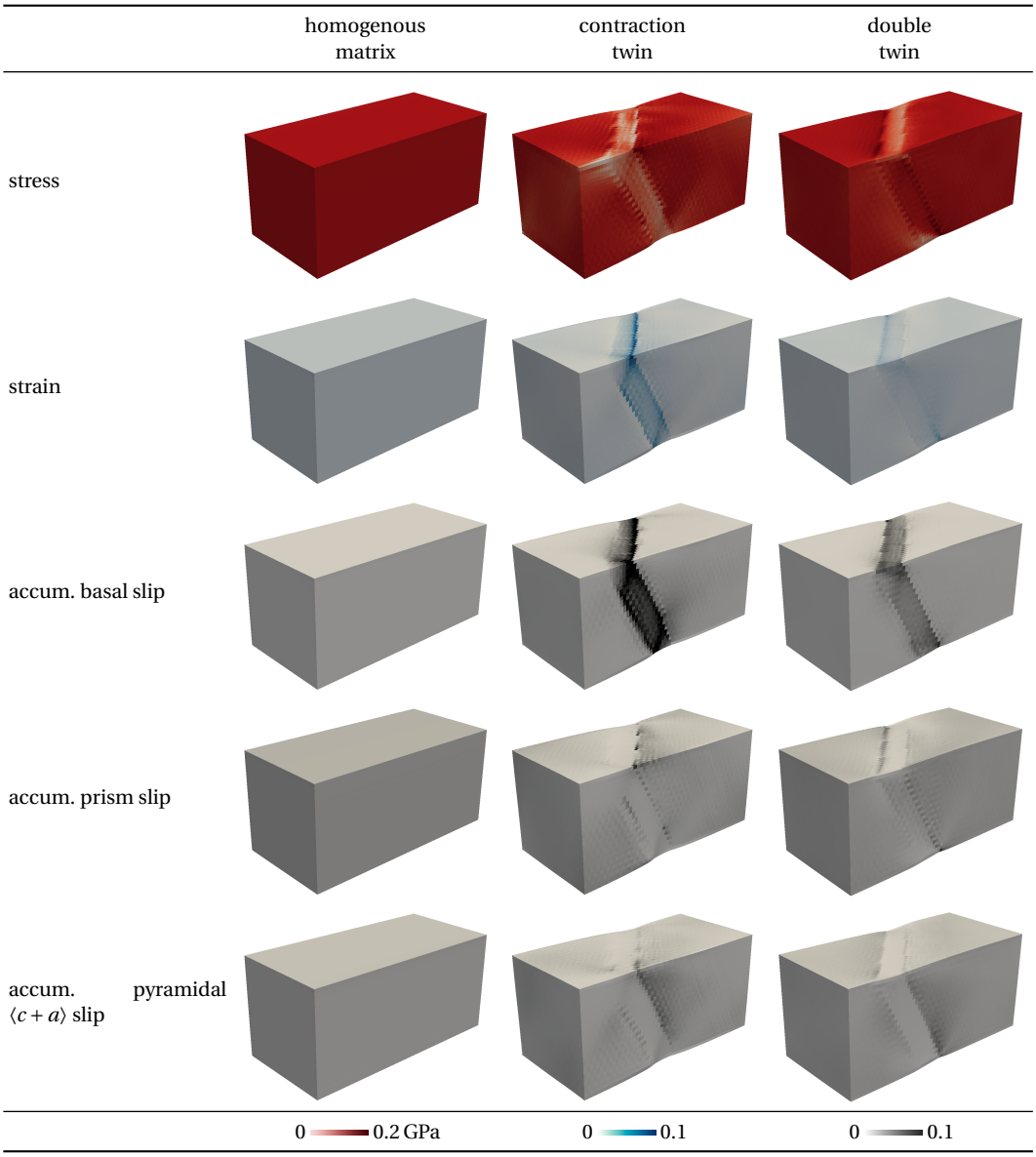

Fig. 12 – Crystal plasticity simulation results of a fixed-width central region sandwiched between a matrix single crystal mimicking the twinned volume shown in the bottom right of Fig. 8 in terms of unidirectional stress, strain, and accumulated shear strain on basal, prismatic, and pyramidal pyramidal $\langle c+a \rangle$ slip families (top to bottom) with different lattice orientations assigned to the central region (left to right).

side of the twin is elevated compared to the matrix on the left.

Strain localization within the twinned volume led to global as well as local incompatibility. The stress concentrations observed in Fig. 12 close to the twin boundary for both twin types might lead to the nucleation of cracks along the matrix–twin interface. This is consistent with the previous experimental studies in which micro-cracks at the $\{1\,0\,\bar{1}\,1\}$–$\{1\,0\,\bar{1}\,2\}$ twin–matrix interface were detected using electron microscopy [22,52]. This could then explain the orientation of the cracks observed in this study, see Fig. 8 (bottom left), i.e. they were parallel to the contraction twin traces suggesting crack nucleation along the matrix–twin interface. Final failure would result when sufficiently many local cracks coalesce as suggested by Fig. 8 (top). Therefore, a certain population of initially twinned volumes is necessary to embrittle the material to an extent that notably reduces ε_f. It appears that such a threshold is reached when the temperature is low enough such that the overall twin activity contributes about 3/4 of the observed deformation activity, since the corresponding ε_f is about 10 % (locally), but no failure is observed despite a strain of 16 % (locally) when twinning accounts for only about 0.2 of the observed deformation activity (see Fig. 7).

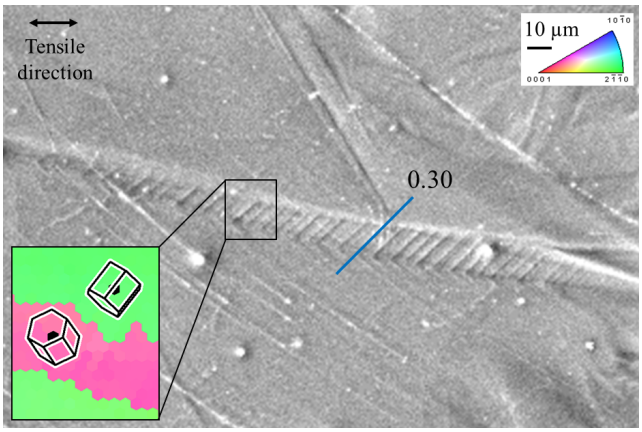

Fig. 13 – The confined slip activity within an extension twinned volume (see inset EBSD IPF map for orientation) was aligned with blue trace of basal slip system having global Schmid factor of 0.30. This observation was made on an as-cast Mg-1Mn-0.5Nd (wt.%) tensile tested at 323 K to 8 % strain [51].

5 Conclusion

1. In-situ tensile experiments, combining EBSD with SEM observations, provided a useful means to quantify the temperature dependence and activity of the various deformation modes.
2. At ambient temperature, mechanical twinning contributed a large fraction to the observed deformation modes, while at higher temperatures, an almost equal fraction of basal, prismatic, and pyramidal $\langle c+a \rangle$ slip accounted for the observed deformation activity.
3. With increasing temperature, the activity of contraction twinning, as a means to accommodate $\langle c+a \rangle$ slip, decreased relative to that of pyramidal $\langle c+a \rangle$ slip, which suggests a stronger decrease of the CRSS for pyramidal $\langle c+a \rangle$ slip compared with contraction twinning with increasing temperature.
4. Contraction twins, which were always partly consumed by $\{10\bar{1}1\}$–$\{10\bar{1}2\}$ double twinning, significantly influenced the ε_f at 323 K.
5. Crystal plasticity modeling and simulations of the deformation behavior of contraction twins and $\{10\bar{1}1\}$–$\{10\bar{1}2\}$ double twins showed localized deformation within the twinned volume due to the enhanced activity of basal slip. In addition, the twin–matrix interfaces were identified to be potential crack initiation sites.
6. Ambient temperature deformation produces a sufficiently large population of contraction twinning and $\{10\bar{1}1\}$–$\{10\bar{1}2\}$ double twinning that initiates crack formation, and this results in low formability compared to elevated temperature deformation.

Acknowledgements

This work was supported by the National Science Foundation through grants DMR-1107117 and CMMI-1463006. The authors also acknowledge Drs. María Teresa Pérez Prado and Javier Llorca of IMDEA Materials Institute (Madrid, Spain) and Thomas R. Bieler of Michigan State University for useful discussions.

References

1. M. M. Avedesian and H. Baker (eds.): *ASM specialty handbook: Magnesium and magnesium alloys*. ASM International, Materials Park, Ohio, 1999.
2. B. Mordike and T. Ebert: *Materials Science and Engineering A*, 2001. vol. 302(1), pp. 37–45. doi:10.1016/S0921-5093(00)01351-4.
3. M. H. Yoo: *Metallurgical Transactions A*, 1981. vol. 12A, pp. 409–418. doi:10.1007/BF02648537.
4. W. H. Hartt and R. E. Reed-Hill: *Transactions of the Metallurgical Society of AIME*, 1967. vol. 239, pp. 1511–1517.
5. R. E. Reed-Hill and W. D. Robertson: *Acta Metallurgica*, 1957. vol. 5(12), pp. 728–737. doi:10.1016/0001-6160(57)90075-5.
6. R. E. Reed-Hill and W. D. Robertson: *Acta Metallurgica*, 1957. vol. 5(12), pp. 717–727. doi:10.1016/0001-6160(57)90074-3.
7. H. Yoshinaga and R. Horiuchi: *Transactions of the Japan Institute of Metals*, 1963. vol. 4(1), pp. 1–8. doi:10.2320/matertrans1960.4.1.
8. H. Yoshinaga, T. Obara, and S. Morozumi: *Materials Science and Engineering*, 1973. vol. 12(5), pp. 255–264.
9. E. W. Kelley and W. F. Hosford: *Transactions of the Metallurgical Society of AIME*, 1968. vol. 242(1), pp. 5–13.
10. B. C. Wonsiewicz and W. A. Backofen: *Transactions of the Metallurgical Society of AIME*, 1967. vol. 239, pp. 1422–1431.
11. W. H. Hartt and R. E. Reed-Hill: *Transactions of the Metallurgical Society of AIME*, 1968. vol. 242, pp. 1127–1133.
12. S. L. Couling, J. F. Pashak, and L. Sturkey: *American Society for Metals Transactions*, 1959. vol. 51, pp. 94–107.
13. J. Bohlen, S. Yi, D. Letzig, and K. U. Kainer: *Materials Science and Engineering: A*, 2010. vol. 527(26), pp. 7092–7098. doi:10.1016/j.msea.2010.07.081.
14. W. B. Hutchinson and M. R. Barnett: *Scripta Materialia*, 2010. vol. 63(7), pp. 737–740. doi:10.1016/j.scriptamat.2010.05.047.
15. A. Chapuis and J. H. Driver: *Acta Materialia*, 2011. vol. 59(5), pp. 1986–1994. doi:10.1016/j.actamat.2010.11.064.
16. K. Yoshida: *International Journal of Plasticity*, 2016. vol. 84, pp. 102–137. doi:10.1016/j.ijplas.2016.05.004.
17. M. R. Barnett, M. D. Nave, and C. J. Bettles: *Materials Science and Engineering: A*, 2004. vol. 386(1-2), pp. 205–211. doi:10.1016/j.msea.2004.07.030.
18. M. D. Nave and M. R. Barnett: *Scripta Materialia*, 2004. vol. 51(9), pp. 881–885. doi:10.1016/j.scriptamat.2004.07.002.
19. G. Martin, C. W. Sinclair, W. J. Poole, and H. Azizi-Alizamini: *JOM*, 2015. vol. 67(8), pp. 1761–1773. doi:10.1007/s11837-015-1449-x.
20. M. R. Barnett: *Materials Science and Engineering: A*, 2007. vol. 464(1-2), pp. 8–16. doi:10.1016/j.msea.2007.02.109.
21. M. R. Barnett, Z. Keshavarz, A. G. Beer, and X. Ma: *Acta Materialia*, 2008. vol. 56(1), pp. 5–15. doi:10.1016/j.actamat.2007.08.034.
22. D. Ando and Y. Sutou: *Acta Materialia*, 2010. vol. 58(13), pp. 4316–4324. doi:10.1016/j.actamat.2010.03.044.

23. D. Ando, J. Koike, and Y. Sutou: *Materials Science and Engineering: A*, 2014. vol. 600, pp. 145–152. doi:10.1016/j.msea.2014.02.010.
24. S. Niknejad, S. Esmaeili, and N. Y. Zhou: *Acta Materialia*, 2016. vol. 102, pp. 1–16. doi:10.1016/j.actamat.2015.09.026.
25. L. Jiang, J. J. Jonas, A. A. Luo, A. K. Sachdev, and S. Godet: *Scripta Materialia*, 2006. vol. 54(5), pp. 771–775. doi:10.1016/j.scriptamat.2005.11.029.
26. Q. Ma, H. El Kadiri, A. L. Oppedal, J. C. Baird, M. F. Horstemeyer, and M. Cherkaoui: *Scripta Materialia*, 2011. vol. 64(9), pp. 813–816. doi:10.1016/j.scriptamat.2011.01.003.
27. Q. Ma, H. El Kadiri, A. L. Oppedal, J. C. Baird, B. Li, M. F. Horstemeyer, and S. C. Vogel: *International Journal of Plasticity*, 2012. vol. 29, pp. 60–76. doi:10.1016/j.ijplas.2011.08.001.
28. D. Ando and J. Koike: *Journal of the Japan Institute of Metals*, 2007. vol. 71(9), pp. 684–687.
29. J. Koike: *Metallurgical and Materials Transactions A*, 2005. vol. 36(7), pp. 1689–1696. doi:10.1007/s11661-005-0032-4.
30. T. Obara, H. Yoshinga, and S. Morozumi: *Acta Metallurgica*, 1973. vol. 21(7), pp. 845–853. doi:10.1016/0001-6160(73)90141-7.
31. A. Chakkedath and C. J. Boehlert: *JOM*, 2015. vol. 67(8), pp. 1748–1760.
32. C. J. Boehlert, Z. Chen, A. Chakkedath, I. Gutiérrez-Urrutia, J. Llorca, J. Bohlen, S. Yi, D. Letzig, and M. T. Pérez-Prado: *Philosophical Magazine*, 2013. vol. 93(6), pp. 598–617. doi:10.1080/14786435.2012.725954.
33. A. Chakkedath, J. Bohlen, S. Yi, D. Letzig, Z. Chen, and C. J. Boehlert: *Metallurgical and Materials Transactions A*, 2014. vol. 45(8), pp. 3254–3274. doi:10.1007/s11661-013-2143-7.
34. A. Chakkedath, S. Yi, D. Letzig, Z. Chen, and C. J. Boehlert: In *Magnesium Technology 2015*. pp. 109–114.
35. C. J. Boehlert, Z. Chen, I. Gutiérrez-Urrutia, J. Llorca, and M. T. Pérez-Prado: *Acta Materialia*, 2012. vol. 60(4), pp. 1889–1904. doi:10.1016/j.actamat.2011.10.025.
36. Z. Chen and C. J. Boehlert: *JOM*, 2013. vol. 65(9), pp. 1237–1244. doi:10.1007/s11837-013-0672-6.
37. C. J. Boehlert, H. Li, L. Wang, and B. Bartha: *Advanced Materials & Processes*, 2010. vol. 168(11), pp. 41–45.
38. H. Li, C. J. Boehlert, T. R. Bieler, and M. A. Crimp: *Philosophical Magazine*, 2015. vol. 95(7), pp. 691–729. doi:10.1080/14786435.2014.1001459.
39. I. Dastidar, A. Pilchak, T. R. Bieler, V. Khademi, M. A. Crimp, and C. J. Boehlert: *Materials Science and Engineering A*, 2015. vol. 636, pp. 289–300.
40. H. Li, D. E. Mason, T. R. Bieler, C. J. Boehlert, and M. A. Crimp: *Acta Materialia*, 2013. vol. 61(20), pp. 7555–7567. doi:10.1016/j.actamat.2013.08.042.
41. F. Roters, P. Eisenlohr, L. Hantcherli, D. D. Tjahjanto, T. R. Bieler, and D. Raabe: *Acta Materialia*, 2010. vol. 58, pp. 1152–1211. doi:10.1016/j.actamat.2009.10.058.
42. F. Roters, P. Eisenlohr, C. Kords, D. D. Tjahjanto, M. Diehl, and D. Raabe: In O. Cazacu (ed.), *Procedia IUTAM: IUTAM Symposium on Linking Scales in Computation: From Microstructure to Macroscale Properties*, vol. 3. Elsevier, Amsterdam, pp. 3–10. doi:10.1016/j.piutam.2012.03.001.
43. D. Peirce, R. J. Asaro, and A. Needleman: *Acta Metallurgica*, 1982. vol. 30(6), pp. 1087–1119. doi:10.1016/0001-6160(82)90005-0.
44. J. W. Hutchinson: *Proceedings of the Royal Society A*, 1976. vol. 348, pp. 101–127. doi:10.1098/rspa.1976.0027.
45. S. R. Agnew, D. Brown, and C. N. Tomé: *Acta Materialia*, 2006. vol. 54(18), pp. 4841–4852. doi:10.1016/j.actamat.2006.06.020.
46. A. Pandey, F. Kabirian, J-H Hwang, S-H Choi, and A. S. Khan: *International Journal of Plasticity*, 2015. vol. 68, pp. 111–131. doi:10.1016/j.ijplas.2014.12.001.
47. A. S. Khan, A. Pandey, T. Gnäupel-Herold, and R. K. Mishra: *International Journal of Plasticity*, 2011. vol. 27(5), pp. 688–706. doi:10.1016/j.ijplas.2010.08.009.
48. ASTM International: *ASTM E112-13 Standard Test Methods for Determining Average Grain Size*, 2013. doi:10.1520/E0112.
49. J. Koike, Y. Sato, and D. Ando: *Materials Transactions*, 2008. vol. 49(12), pp. 2792–2800. doi:10.2320/matertrans.MRA2008283.
50. H. Yoshinaga and R. Horiuchi: *Transactions of the Japan Institute of Metals*, 1964. vol. 5(1), pp. 14–21.
51. A. Chakkedath: *A study of the effects of rare-earth elements on the microstructural evolution and deformation behavior of magnesium alloys at temperatures up to 523K*. Ph.D. thesis, Michigan State University, 2016. URL `https://search.proquest.com/docview/1776157968?accountid=12598`.
52. P. Cizek and M. R. Barnett: *Scripta Materialia*, 2008. vol. 59(9), pp. 959–962. doi:10.1016/j.scriptamat.2008.06.041.